

# Polarized Raman of Nanoscale Two-Dimensional Materials: Combined Optical and Structural Effects

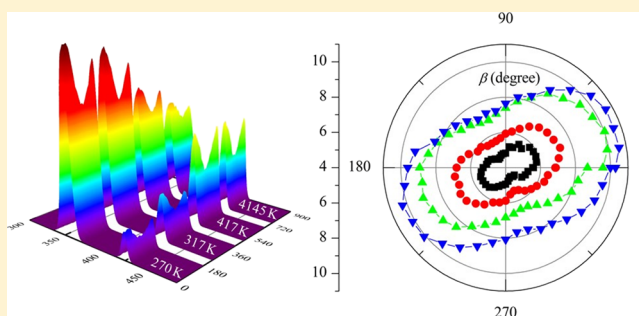
Hamidreza Zobeiri,<sup>†,||</sup> Ridong Wang,<sup>†,||</sup> Cheng Deng,<sup>§</sup> Qianying Zhang,<sup>\*,‡</sup> and Xinwei Wang<sup>\*,†</sup>

<sup>†</sup>Department of Mechanical Engineering, Iowa State University, Ames, Iowa 50011, United States

<sup>‡</sup>College of Metallurgy and Material Engineering, Chongqing University of Science & Technology, University Town, Huxi Shapingba District, Chongqing 401331, P. R. China

<sup>§</sup>College of Mechatronics Engineering, Guangdong Polytechnic Normal University, Guangzhou 510635, People's Republic of China

**ABSTRACT:** The intensity response of polarized Raman is studied using backscattered Raman spectroscopy. In previous works, it was confirmed that the Raman intensities of the  $E_{2g}^1$  modes for  $WS_2$  and  $MoS_2$  as well as the G mode of graphene are independent of the polarization angle. However, a strong correlation is found between them in this work using a confocal Raman system. The  $E_{2g}^1$  and  $A_{1g}$  modes of nanometer-thick  $WS_2$  and  $MoS_2$  samples as well as the G mode of bulk graphene are used to investigate the polarization dependency of the Raman intensity for each mode. Additionally, the effects of temperature and sample structure on the Raman intensity are studied using the  $WS_2$  sample on both suspended and supported areas. Results of these experiments are explained and fitted by the theoretical Raman intensity profiles. This theoretical study is conducted using the classical theory of polarized Raman spectroscopy and includes all the information about polarization of excitation laser, rotation of the beam splitter, and different vibrational modes of samples, which is considered in Raman tensors. It is concluded that Raman intensity variation with incident laser polarization not only is a function of the material structure but also carries information about the optical functionality of the Raman system.



## 1. INTRODUCTION

Raman spectroscopy is becoming a powerful tool to characterize the thermal, charge carrier, and structural properties of materials. Raman spectroscopy can provide information about the electronic structures,<sup>1,2</sup> lattice vibration and crystallographic orientations,<sup>3–7</sup> hot carrier and thermal transport,<sup>8–10</sup> and charge transfer of these materials.<sup>11,12</sup> One of the techniques that probe information about the crystal orientation and symmetry of bond vibrations is polarized Raman spectroscopy. It is a promising technique for polarization measurement since the lasers used for excitation are naturally linearly polarized.

Polarized Raman spectroscopy could be conducted using different typical setups based on polarization of incident or scattered light or rotation of the sample. In one configuration, only the incident laser light is polarized while the analyzer is held constant, and scattered light is not polarization-controlled before entering the spectrometer.<sup>13,14</sup> In another configuration, polarization of incident light is either vertical or horizontal, while the polarization of the scattered light is tuned by an analyzer.<sup>3,15,16</sup> It is possible to combine the last two configurations and control the polarization of the incident and scattered lights simultaneously. If the polarizer is inserted in the path of incident and scattered laser lights, they will be both polarized in a similar direction. By using two polarizers, it is possible to polarize both lights in separate directions.<sup>17,18</sup>

While the aforementioned setups are adjusted by the position of the polarizer, another possible configuration could be rotating the sample around the laser beam, while the polarization of incident and scattered lights is constant.<sup>19,20</sup>

Polarization measurements could be used to identify the crystal orientations of several ordered materials. Wang et al. developed the optothermal Raman spectroscopy (OT-Raman) method to identify the crystalline orientation of black phosphorus (BP).<sup>14</sup> They could identify the crystalline orientation of BP regardless of sample thickness and excitation wavelength using Raman frequency-power differential  $\Phi = \partial\omega/\partial P$ .  $\Phi$  is minimum (maximum) when laser polarization is along the zigzag (armchair) direction. Duesberg et al. performed polarized micro-Raman spectroscopy on spatially separated single-wall CNTs, and it revealed that, when nanotubes are aligned parallel to the polarization of the incident light, the intensities of all Raman modes are maximum.<sup>21</sup> Zhang et al. determined the crystalline orientation of phosphorene flakes without tunneling electron microscopy by polarized Raman spectroscopy.<sup>22</sup> Wang et al. used polarized micro-Raman spectroscopy to study the crystallographic orientation of monolayer  $MoS_2$  under controllable uniaxial tensile strain.<sup>3</sup>

Received: July 19, 2019

Revised: August 23, 2019

Published: August 28, 2019

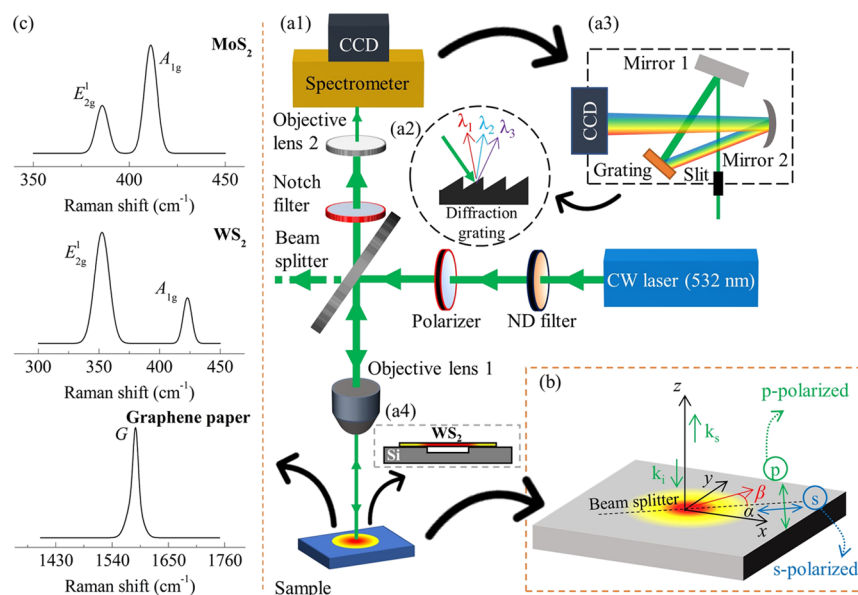


**Figure 1.** (a1) Schematic of polarized Raman system. The suspended or supported sample is irradiated by the 532 nm CW laser. Laser power and polarization of the incident beam are controlled by the ND filter and polarizer, respectively. (a2) Diffraction grating splits and diffracts laser light in different wavelengths. (a3) Different components inside the spectrometer. The laser beam is diffracted by grating and reflected onto the CCD sensor by the concave mirror (mirror 2). The CCD detector converts the photons to electrons, which are digitized to a computer. (a4) Prepared suspended WS<sub>2</sub> sample by mechanical exfoliation technique. MoS<sub>2</sub> and graphene paper samples are transferred similar to the bare Si substrate. (b) Definition of the incident polarization angle ( $\beta$ ) and angle of rotation of beam splitter about the z axis ( $\alpha$ ). s- and p-polarized directions are parallel and normal to the direction of the beam splitter, which is shown by the black dashed line. Here, the  $x$ - $y$  coordinate is attached to the sample structure. (c) Raman spectra of MoS<sub>2</sub>, WS<sub>2</sub>, and graphene paper excited by the CW laser. The  $E_{2g}^1$  and  $A_{1g}$  Raman modes of WS<sub>2</sub> and MoS<sub>2</sub> and G peak of graphene paper are observed.

They showed that the doubly degenerate  $E_{2g}^1$  mode splits into two modes, namely,  $E_{2g}^{1+}$  and  $E_{2g}^{1-}$ . The intensities of these submodes respond to the angle between the strain axis and polarization of the scattered light, orthogonally. Ribeiro et al. studied the angular dependence of polarized Raman spectra for the  $A_g^1$ ,  $A_g^2$ , and  $B_{2g}$  modes in both parallel and cross-polarization configurations using three different lasers with three wavelengths and concluded that Raman tensors exhibit complex elements.<sup>23</sup> They measured the phase difference between each laser line and Raman tensor elements for each mode and observed that phase differences are much smaller for the out-of-plane  $A_g^1$  mode than for the in-plane totally symmetric  $A_g^2$  mode.

In this work, we study the intensity response of polarized Raman using a confocal Raman system. Both  $E_{2g}^1$  and  $A_{1g}$  Raman modes of WS<sub>2</sub> and MoS<sub>2</sub> and G mode of graphene paper are used to analyze the responses of Raman and optical systems. Also, this analysis is conducted at different temperatures for the WS<sub>2</sub> sample on both suspended and supported areas. It is discovered that the final Raman intensity variation with excitation laser polarization cannot be simply interpreted as the structural effect, but rather it includes information about the optical system.

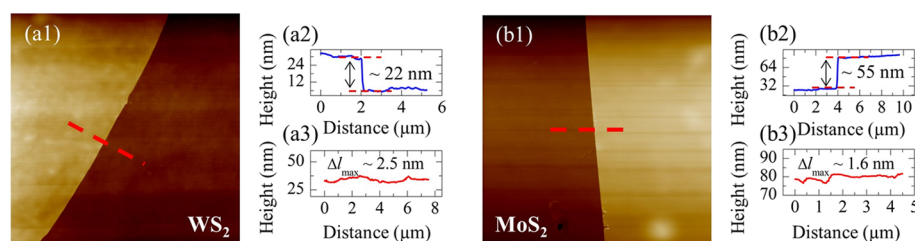
## 2. EXPERIMENTAL SECTION

Figure 1a1 shows the polarized Raman configuration used in this work. The measurements are conducted at room temperature or other temperatures using a BWTEK Voyage confocal Raman system. Raman spectra are excited using a continuous wave (CW) laser with 532 nm wavelength (Excelsior-532-150-CDRH, Spectra-Physics) and collected in the backscattering configuration. A neutral density (ND) filter is used to adjust the laser power, and a half-wave plate is

applied to adjust the polarization of the incident beam. After passing the ND filter and polarizer, the laser beam goes through the beam splitter and part of that is reflected and focused on the sample using a 20 $\times$  objective lens. The temperature of the sample is controlled by an optical cell chamber. The chamber is filled by N<sub>2</sub> gas and rapid inlet and outlet of N<sub>2</sub> to control the temperature. This chamber is not shown in Figure 1. More information about it can be found in our previous work.<sup>24</sup> The rest of the laser beam is transmitted through the beam splitter, which is shown using the dotted line. The scattered Raman signal from the sample transmits through the beam splitter and after passing the notch filter is focused using a second objective lens onto the slit of the spectrometer. A notch filter is used to block the reflected laser beam. Then the Raman signal is directed onto the diffraction grating using a mirror. The grating disperses the spectral components of the Raman light at slightly varying angles, which determines the optical resolution and wavelength range that the spectrometer achieves, as shown in Figure 1a2. Finally, the dispersed light is focused by another mirror and imaged onto the CCD detector (Figure 1a3). More details about our Raman system and its components can be found in our previous works.<sup>8,25</sup> Figure 1c shows the Raman spectra of WS<sub>2</sub>, MoS<sub>2</sub>, and graphene paper. In this work, we use the  $E_{2g}^1$  and  $A_{1g}$  peaks of MoS<sub>2</sub> and WS<sub>2</sub> and the G peak of graphene paper to perform our analysis.

## 3. RESULTS AND PHYSICS

**3.1. Polarized Raman of WS<sub>2</sub>: Experimental Observation.** Few-layered WS<sub>2</sub>, MoS<sub>2</sub>, and graphene paper samples are prepared by the mechanical exfoliation and transfer method. Mechanical exfoliation is one of the most successful techniques to obtain few-layered nanocrystals with high quality from bulk



**Figure 2.** AFM measurement of WS<sub>2</sub> and MoS<sub>2</sub> samples. (a1,b1) AFM images of two samples. (a2,b2) Thickness profile of each sample corresponding to the red dashed line in AFM images. (a3,b3) Thickness profiles that indicate the roughness of samples. For both samples, roughness is less than 10% of total thickness.

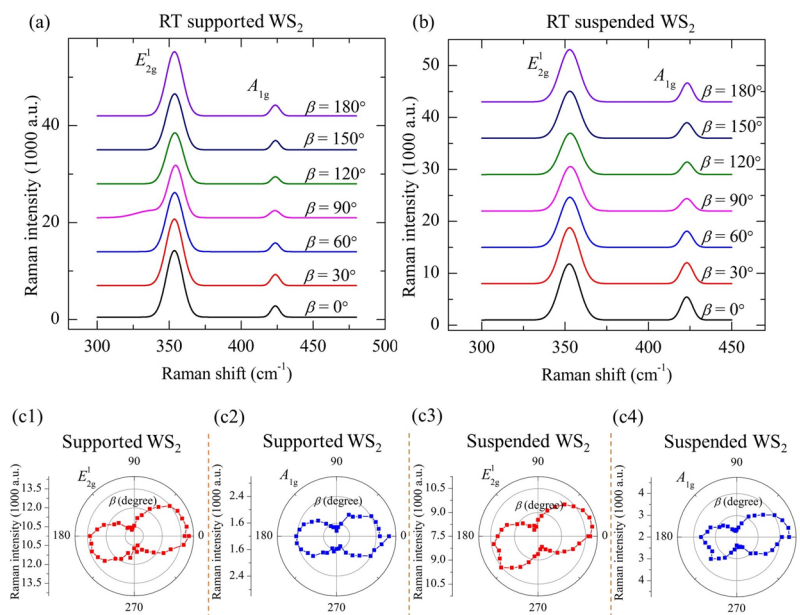


**Figure 3.** (a,b) Room-temperature Raman spectra of 22 nm thick WS<sub>2</sub> sample on both supported and suspended areas at different polarization angles, respectively. (c1–c4) Polar plots of Raman intensities of WS<sub>2</sub> sample at room temperature. As shown in this figure, the Raman intensities of both E<sub>2g</sub><sup>1</sup> and A<sub>1g</sub> peaks reach their minimum when  $\beta$  is around 100 or 280°.

layered structures. First, a thick layer of material is peeled off from the bulk structure using Scotch tape. Then this layer is transferred to a gel film. Exfoliation using the gel film is conducted several times to achieve the desired thickness of the few-layered sample. After finding the desired area, the sample is transferred to a silicon substrate with a hole in it. The hole diameter is 10  $\mu\text{m}$ , and its depth is 3  $\mu\text{m}$ . A side view of this sample is shown in Figure 1a4, showing both suspended and supported areas. Only the WS<sub>2</sub> sample is transferred to the substrate with the hole to investigate the effects of the substrate on the polarized Raman intensity and the area near the hole used as the supported area. Only the supported area is used for two other materials.

Figure 2 shows the AFM images of WS<sub>2</sub> and MoS<sub>2</sub> samples. To perform the AFM measurement, we use the supported area of each sample to avoid damaging the suspended area. The thicknesses of WS<sub>2</sub> and MoS<sub>2</sub> samples are 22 and 55 nm, respectively. As shown in Figure 2a3,b3, the roughness profile of each sample is measured as the biggest thickness variation ( $\Delta I_{\text{max}}$ ) along a line on the sample surface.  $\Delta I_{\text{max}}$  is larger for the WS<sub>2</sub> sample, which may be due to wrinkles on it. In this work, we used bulk graphene paper to perform the Raman experiment; therefore, AFM measurement is not conducted for this sample.

The 532 nm wavelength CW laser that is used in this work is vertically polarized with a polarization ratio of more than 100:1. Therefore, if a beam splitter is not rotated about the  $z$  axis, the incident laser that is reflected by beam splitter and irradiates the sample will be polarized along the  $y$ -axis direction (as shown in Figure 1b). However, in reality, the beam splitter is rotated about the  $z$  axis slightly. Here, this effect is considered in detail, and we take the beam splitter rotation angle as  $\alpha$  about the  $z$  axis (Figure 1b). In fact,  $\alpha$  is the angle between the projection of the rotated beam splitter onto the  $x$ - $y$  plane and the  $x$  axis. Based on this configuration, polarization of both incident and scattered lights could be evaluated in both s-polarized (along the beam splitter) and p-polarized (normal to the beam splitter) directions. In Figure 1b,  $k_i$  and  $k_s$  represent the incident and scattered wave vectors, respectively, and both are along the  $z$  direction. Additionally,  $\beta$  indicates the polarization angle of incident light generated by the polarizer.

In some Raman experiments, the photon energy used for crystal excitation corresponds to a real electronic transition in a crystal. In this case, the scattered Raman intensity will be enhanced. Such a phenomenon is called resonant Raman scattering. For WS<sub>2</sub>, the excitonic gap for the B exciton is 2.33 eV at room temperature, which is very close to the photon energy of the 532 nm laser. Excitonic energy increases with

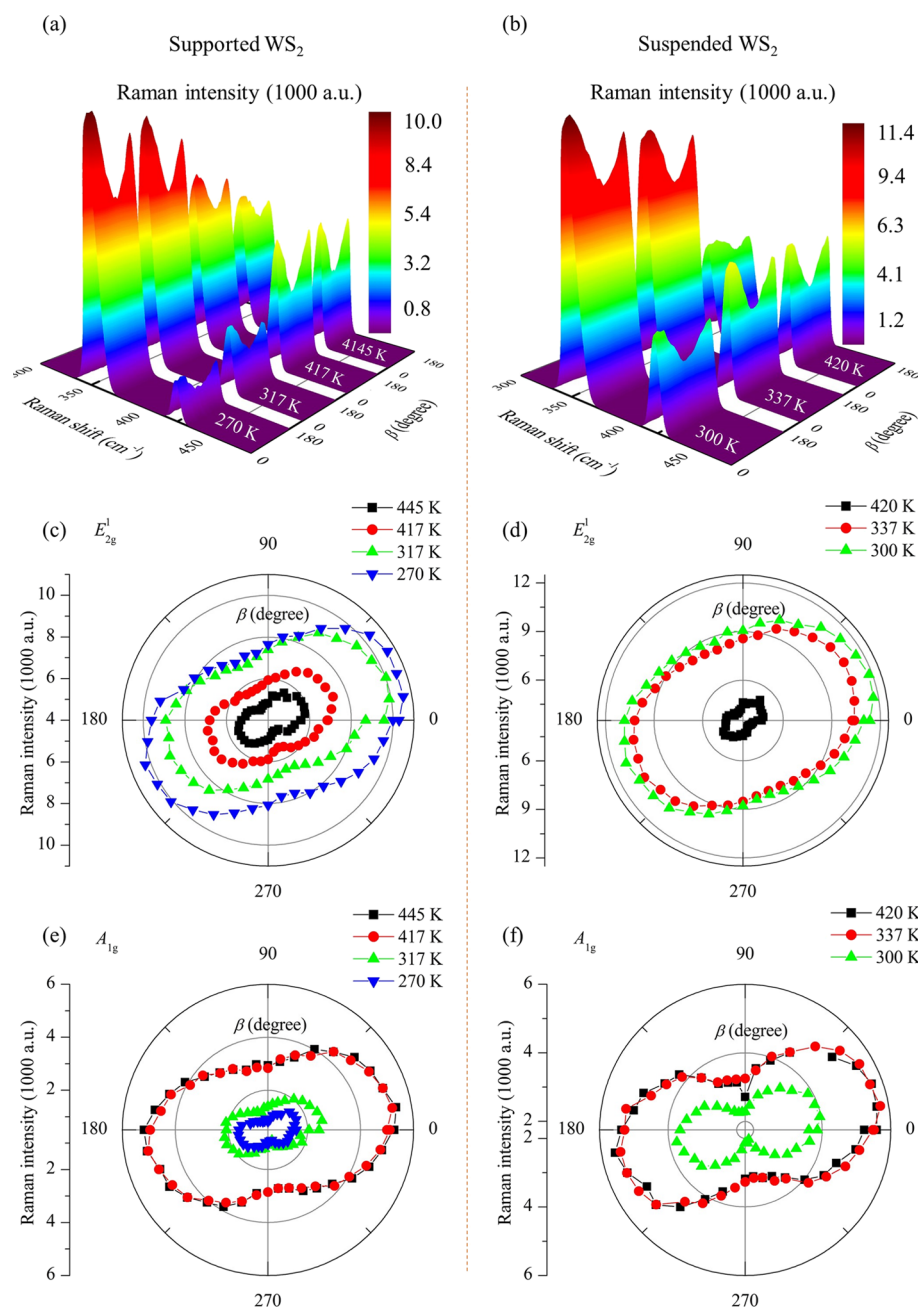


**Figure 4.** (a,b) 3D contour maps of WS<sub>2</sub> Raman peaks for supported and suspended areas, respectively. This contour shows the variation of Raman intensity against polarization angle in the range of 0 to 180° at different temperatures. Generally, near 350 K, resonant Raman scattering happens and Raman intensity reaches the maximum. (c–f) Polar plots of temperature-dependent polarized Raman intensities of WS<sub>2</sub> sample.

increasing temperature and is far away from the photon energy. Therefore, resonant Raman scattering is expected to happen in our experiment at temperatures close to the room temperature. Again, for the WS<sub>2</sub> sample, the energy of excitons is almost resonant to the photon energy of 532 nm laser as the temperature of the sample is set at ~330 K.<sup>26</sup>

As mentioned earlier, the polarized Raman experiment of the WS<sub>2</sub> sample is conducted at room temperature as well as other temperatures using both supported and suspended areas. Figure 3a,b shows seven representative Raman spectra of WS<sub>2</sub> at room temperature and various polarization angles ( $\beta$ ) for both supported and suspended areas, respectively. Figure 3c1–c4 shows the polar plots of Raman intensities of both modes as  $\beta$  is varied from 0 to 360°. It is obvious from this figure that

the intensities of both Raman peaks are maximum when  $\beta$  is either around 15 or 195° and are minimum when  $\beta$  is around 100 or 280°. In addition, this experiment is conducted at several temperatures to investigate the effect of temperature on the polarized Raman intensity. These temperatures are selected in the range of lower and higher than room temperature at which resonant Raman occurs. Figure 4 shows the result of this experiment. As shown in Figure 4a by the 3D contour map of WS<sub>2</sub> Raman peaks at several temperatures and polarization angles, as the temperature of supported WS<sub>2</sub> increases from 270 to 445 K at all polarization angles ( $\beta$ ), the Raman intensity of the E<sub>2g</sub><sup>1</sup> peak decreases and is maximum at 270 K when the B exciton energy is equal to the laser photon energy. Note that laser power and laser integration time during the experiment

for all above temperatures are held unchanged as 5 mW and 2 s, respectively. Meanwhile, for the  $A_{1g}$  peak, the resonance temperature is higher than the  $E_{2g}^1$  peak and is around 410 K. Similar trends are observed using the suspended  $WS_2$  sample (Figure 4b). Differences between the resonance temperatures of the two peaks could be caused by the effect of the 2LA(M) peak on data fitting of the  $E_{2g}^1$  mode. The vibrational frequencies of the  $E_{2g}^1$  and 2LA(M) modes are very close, and these two peaks overlap with each other.<sup>27</sup> Therefore, it is not possible to distinguish both peaks exactly using our Raman spectrometer with a spectral resolution of  $1.9\text{ cm}^{-1}$  at wavenumbers close to the location of the  $E_{2g}^1$  and 2LA(M) peaks. Additionally, comparing Figure 4a,b, we can see that the resonance temperature of the suspended sample is lower than that of the supported one. This is caused by a higher temperature rise of the suspended sample under the same laser irradiation. Figure 4c–f represents the same information but in the form of a polar plot. Again, for both Raman peaks, the intensity is highest at angles near  $10$  or  $190^\circ$ .

**3.2. Physics: Combined Structural and Optical Effects.** Contrary to the above observed  $E_{2g}^1$  intensity variation with the polarization angle, in previous works, it has been documented that the Raman intensity of the  $E_{2g}^1$  mode is independent of the polarization angle of the incident light.<sup>3,28</sup> However, the beam splitter does not have exactly similar reflectivity and transmissivity in s- and p-polarized directions, and they change with respect to  $\beta$ . Additionally, such transmission and reflection change with the light wavelength, which means that transmissivity and reflectivity of the beam splitter for different Raman peaks could be slightly different. In the following, effects of these scenarios on the polarized Raman intensity are investigated to explain our observed Raman intensity variation with the polarization angle.

Here, we explore the Raman intensity of the scattered light by considering all of the aforementioned details. Vectors of incident and scattered photons of both s and p polarizations are defined below

$$e_i^s = A \begin{bmatrix} \cos(\alpha) \\ \sin(\alpha) \\ 0 \end{bmatrix}, e_s^s = C \begin{bmatrix} \cos(\alpha) \\ \sin(\alpha) \\ 0 \end{bmatrix}, e_i^p = B \begin{bmatrix} -\sin(\alpha) \\ \cos(\alpha) \\ 0 \end{bmatrix}, e_s^p = D \begin{bmatrix} -\sin(\alpha) \\ \cos(\alpha) \\ 0 \end{bmatrix} \quad (1)$$

where  $A$  and  $B$  are factors that are reflectivities of the beam splitter in the parallel and normal directions (s and p polarizations) and  $C$  and  $D$  represent the transmissivities of the beam splitter in these two directions, respectively. By doing so, we consider that the beam splitter has different reflection (or transmission) in parallel and normal directions to the beam splitter.

Using the classical theory of the polarized Raman spectrum, we can understand the polarization dependence of the Raman intensity as below

$$I \propto |e_s^t R e_i|^2 \quad (2)$$

where  $R$  describes the Raman tensor of each Raman mode and is represented by a  $3 \times 3$  matrix and  $e_i^t$  is the transpose of the  $e_s$  column vector as defined in eq 1. Using eq 2, the scattered light polarization of the incident light ( $e_i$ ) is measured as  $R e_i$ , and its amplitude observed in the  $e_s$  direction corresponds to the inner product of  $e_s$  and  $R e_i$ . Here, the  $E_{2g}^1$  and  $A_{1g}$  Raman modes are considered to investigate the polarization dependence of the Raman intensity of  $WS_2$ . The  $E_{2g}^1$  mode is doubly

degenerate and corresponds to the in-plane vibrations in the  $x$ - $y$  directions, and the  $A_{1g}$  mode is nondegenerate and corresponds to out-of-plane vibrations of W and S atoms in the  $WS_2$  structure. The Raman tensors of these two modes are

$$R_1^{E_{2g}^1} = \begin{bmatrix} 0 & a & 0 \\ a & 0 & 0 \\ 0 & 0 & 0 \end{bmatrix}, R_2^{E_{2g}^1} = \begin{bmatrix} d & 0 & 0 \\ 0 & -d & 0 \\ 0 & 0 & 0 \end{bmatrix}, R^{A_{1g}} = \begin{bmatrix} b & 0 & 0 \\ 0 & b & 0 \\ 0 & 0 & c \end{bmatrix} \quad (3)$$

where  $a$ ,  $b$ ,  $c$ , and  $d$  are major terms in the Raman tensor matrix and represent the physics of the interaction between crystal lattice and light.<sup>29</sup> As mentioned above, the  $E_{2g}^1$  mode is doubly degenerate, and therefore, it has two Raman tensors, as shown in eq 3.  $R_1^{E_{2g}^1}$  corresponds to the state that polarizability of the lattice is in the  $x$  (or  $y$ ) direction and polarization of the incident light is in the  $y$  (or  $x$ ) direction.  $R_2^{E_{2g}^1}$  corresponds to the in-plane vibrations that the polarizability of the lattice and polarization of the incident light are in the same direction. The G peak of graphene paper has the same Raman tensors as the  $E_{2g}^1$  peak of  $WS_2$  (or  $MoS_2$ ). In most published works, it is assumed that  $a \approx d$ . We perform our analysis based on this assumption, and more discussion about it and its effects on our calculation will be provided in the next sections. The Raman intensities of the  $E_{2g}^1$  mode using two Raman tensors  $R_1^{E_{2g}^1}$  and  $R_2^{E_{2g}^1}$  are calculated as

$$I_{E_{2g}^1}^1 \propto [|(e_s^{s,t} R_1^{E_{2g}^1} e_i^s)| \cos \beta + (e_s^{s,t} R_1^{E_{2g}^1} e_i^p) \sin \beta|^2 + |(e_s^{p,t} R_1^{E_{2g}^1} e_i^s)| \cos \beta + (e_s^{p,t} R_1^{E_{2g}^1} e_i^p) \sin \beta|^2], \\ I_{E_{2g}^1}^2 \propto [|(e_s^{s,t} R_2^{E_{2g}^1} e_i^s)| \cos \beta + (e_s^{s,t} R_2^{E_{2g}^1} e_i^p) \sin \beta|^2 + |(e_s^{p,t} R_2^{E_{2g}^1} e_i^s)| \cos \beta + (e_s^{p,t} R_2^{E_{2g}^1} e_i^p) \sin \beta|^2] \quad (4)$$

where  $I_{E_{2g}^1}^1$  and  $I_{E_{2g}^1}^2$  are the intensities of the  $E_{2g}^1$  peak, which are calculated by  $R_1^{E_{2g}^1}$  and  $R_2^{E_{2g}^1}$ , respectively. For example, the term  $(e_s^{s,t} R_1^{E_{2g}^1} e_i^s) \cos \beta$  is proportional to the Raman intensity of the incident light, which is polarized in the s direction and is calculated using the first Raman tensor of the  $E_{2g}^1$  mode. By substituting eqs 1–3 into eq 4, we can calculate  $I_{E_{2g}^1}^1$  and  $I_{E_{2g}^1}^2$  as

$$I_{E_{2g}^1}^1 \propto (Ca)^2 [A \sin 2\alpha \cos \beta + B \cos 2\alpha \sin \beta]^2 + (Da)^2 [A \cos 2\alpha \cos \beta - B \sin 2\alpha \sin \beta]^2, \\ I_{E_{2g}^1}^2 \propto (Ca)^2 [A \cos 2\alpha \cos \beta - B \sin 2\alpha \sin \beta]^2 + (Da)^2 [-A \sin 2\alpha \cos \beta - B \cos 2\alpha \sin \beta]^2 \quad (5)$$

Therefore, the Raman intensity of the  $E_{2g}^1$  mode is expressed as

$$I_{E_{2g}^1} = I_{E_{2g}^1}^1 + I_{E_{2g}^1}^2 \propto [a^2(C^2 + D^2)][(A \cos \beta)^2 + (B \sin \beta)^2] \quad (6)$$

Similarly, these calculations are conducted to find the polarized-dependent Raman intensity of the  $A_{1g}$  mode using its Raman tensor, and the corresponding result is

$$I_{A_{1g}} \propto b^2 [(AC \cos \beta)^2 + (BD \sin \beta)^2] \quad (7)$$

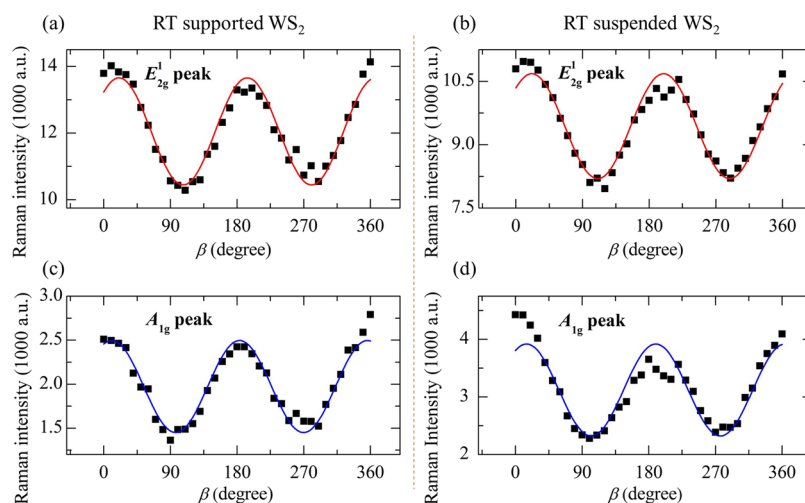


**Figure 5.** Polarization-dependent Raman intensities of  $E_{2g}^1$  and  $A_{1g}$  modes of  $WS_2$  sample at room temperature for both supported and suspended locations. Dots represent the experimental results and are fitted by a sine-squared function. The fitting results are shown by solid lines.

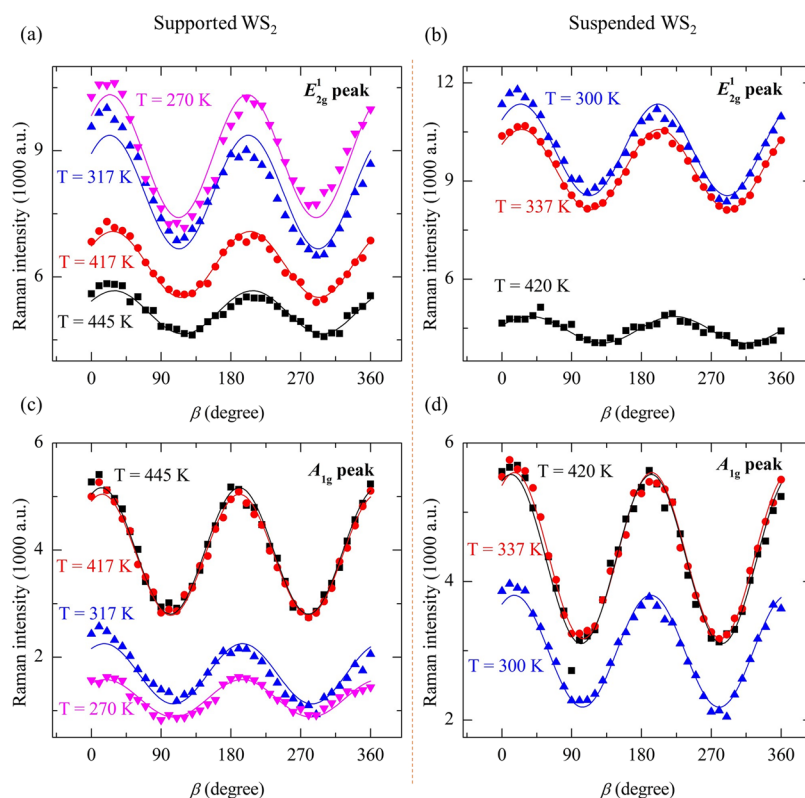


**Figure 6.** Temperature-dependent polarized Raman intensity against  $\beta$  for supported (a,c) and suspended (b,d)  $WS_2$  samples. Dots are experimental data that are fitted by the sine-squared function (solid lines).

To continue our investigation in polarized-dependent Raman intensities of the  $E_{2g}^1$  and  $A_{1g}$  modes, we define two new parameters as  $\psi = B/A$  and  $\delta = D/C$ .  $\psi$  indicates the intensity ratio of the p-polarized photon to s-polarized photon, which are reflected by the beam splitter, and  $\delta$  means the intensity ratio of the p-polarized light to the s-polarized light that are transmitted through the beam splitter. Figure 5 shows the room-temperature  $WS_2$  Raman intensity variation with polarization angle ( $\beta$ ) for both Raman peaks. The dots indicate the experimental data. Experimental data are fitted by a sine-squared function and represented by solid lines in Figure 5. The general form of this function is  $f(\beta) = G\sin^2\beta + K\cos^2\beta$ ,

where  $G$  and  $K$  are fitting constants. By fitting the experimental data of the  $E_{2g}^1$  peak, we obtain  $\psi$  as  $\psi = B/A = \sqrt{G/K}$ . In addition, the ratio of  $G/K$  obtained by fitting the  $A_{1g}$  data represents  $(BD/AC)^2$ , and we define a third parameter as  $\phi = BD/AC$ . Thus,  $\psi$ ,  $\phi$ , and  $\delta$  for the supported or suspended area could be found by fitting  $I$  against  $\beta$  of two peaks. The same calculation is conducted for the temperature-dependent experiment, and its results are shown in Figure 6. Figure 6a,c [or panels (b) and (d)] shows the experimental and fitting results of the temperature-dependent experiment using the supported (or suspended) area. Again, Figure 6 shows the variation in Raman intensity in each temperature, which

confirms the resonant Raman effect at selected temperatures. The measured  $\psi$ ,  $\phi$ , and  $\delta$  for each case are included in Table 1. As mentioned earlier in the Introduction, there are several

**Table 1. Measured  $\psi$ ,  $\phi$ , and  $\delta$  for WS<sub>2</sub> at Different Temperatures and MoS<sub>2</sub> and Graphene Paper Samples at Room Temperature**

| material                                       | T (K) | $\psi$ | $\phi$ | $\delta$ |
|--|-------|--------|--------|----------|
| WS <sub>2</sub> (supported)                    | RT    | 0.874  | 0.762  | 0.872    |
|  | 270   | 0.847  | 0.747  | 0.882    |
|  | 317   | 0.843  | 0.707  | 0.838    |
|  | 417   | 0.882  | 0.742  | 0.841    |
|  | 445   | 0.905  | 0.737  | 0.814    |
| WS <sub>2</sub> (suspended)                    | RT    | 0.876  | 0.769  | 0.879    |
|  | 300   | 0.868  | 0.758  | 0.873    |
|  | 337   | 0.876  | 0.755  | 0.861    |
|  | 420   | 0.912  | 0.748  | 0.819    |
| MoS <sub>2</sub> (supported)<br>graphene paper | RT    | 0.812  | 0.741  | 0.912    |
|  | RT    | 0.885  |        |          |

polarized Raman configurations based on the position of polarizer(s), and these calculations are applicable for those configurations, too. For instance, in a system with a second polarizer that is placed before the spectrometer, it is still necessary to take the optical and structural effects into consideration.

Results of the temperature-dependent experiment using the WS<sub>2</sub> sample on both areas are plotted, as shown in Figure 7, to study the effect of the sample's temperature on  $\psi$ ,  $\phi$ , and  $\delta$ . For both supported and suspended areas,  $\psi$  increases with increasing temperature. Meanwhile, as temperature decreases,  $\delta$  decreases, too. However,  $\phi$  remains almost unchanged and for all cases is around 0.75. Theoretically, all of these three parameters correspond to the optical properties of our Raman system and should not be changed by the sample's physics or its temperature. As we discussed earlier, both E<sub>2g</sub><sup>1</sup> and 2LA(M) modes are present and are overlapping each other. When temperature increases from 300 to 450 K, the 2LA(M) peak becomes weaker and it has less contribution in the combined peak that we use for our data analysis.<sup>27</sup> Additionally,  $\psi$  only depends on A and B, which are measured by fitting this combined mode of E<sub>2g</sub><sup>1</sup> and 2LA(M) modes. Therefore, as shown in Figure 7a,b by black lines,  $\psi$  experiences an increasing trend by increased temperature. On the other hand, as shown by eq 7,  $\phi$  is measured by analyzing the A<sub>1g</sub> peak, and since this peak is not overlapping other Raman peaks, we can fit it very precisely. Thus,  $\phi$  is almost constant for all of the temperatures and both supported and suspended

areas. Finally, since  $\delta$  is calculated as  $\delta = \phi/\psi$ , it decreases against the increased temperature, which is shown by blue lines in Figure 7a,b. These fitting results indicate that transmission and reflectance of the beam splitter for the s- and p-polarized lights are not exactly the same. Ideally for a 50:50 (R:T) beam splitter, the transmission and reflection in either directions should be the same, while in the actual case, they are slightly different. For instance, for a 1 mm thick 50:50 non-polarizing beam splitter (BWS10R, ThorLabs) at 45° incidence, transmission values of s- and p-polarized lights are 41 and 56%, respectively. Additionally, reflection values of s- and p-polarized lights are 57 and 42%, respectively, for this beam splitter. This means that reflection and transmission of s- and p-polarized lights are different, even for a 50:50 non-polarizing beam splitters. As the reflection-to-transmission ratio (R:T) deviates from 50:50, the difference between the transmissivity and reflectivity in each direction becomes even more obvious.

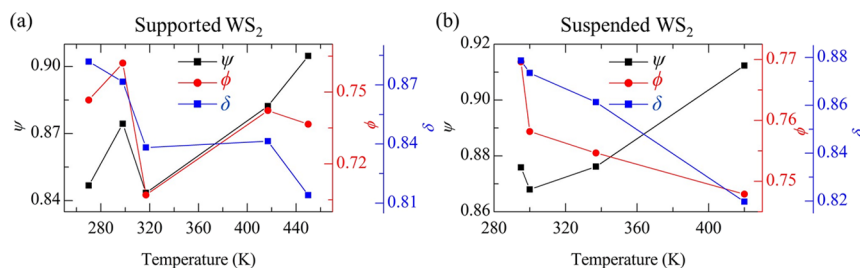
### 3.3. Polarized Raman of MoS<sub>2</sub> and Graphene Paper.

In this section, MoS<sub>2</sub> and graphene paper are used to verify the analysis that was conducted in the last section and provide more explanations. For these two materials, only the room-temperature polarized Raman experiment is conducted. Using our Raman system, both E<sub>2g</sub><sup>1</sup> and A<sub>1g</sub> peaks of MoS<sub>2</sub> as well as the G peak of graphene paper are observed and used to perform the analysis.

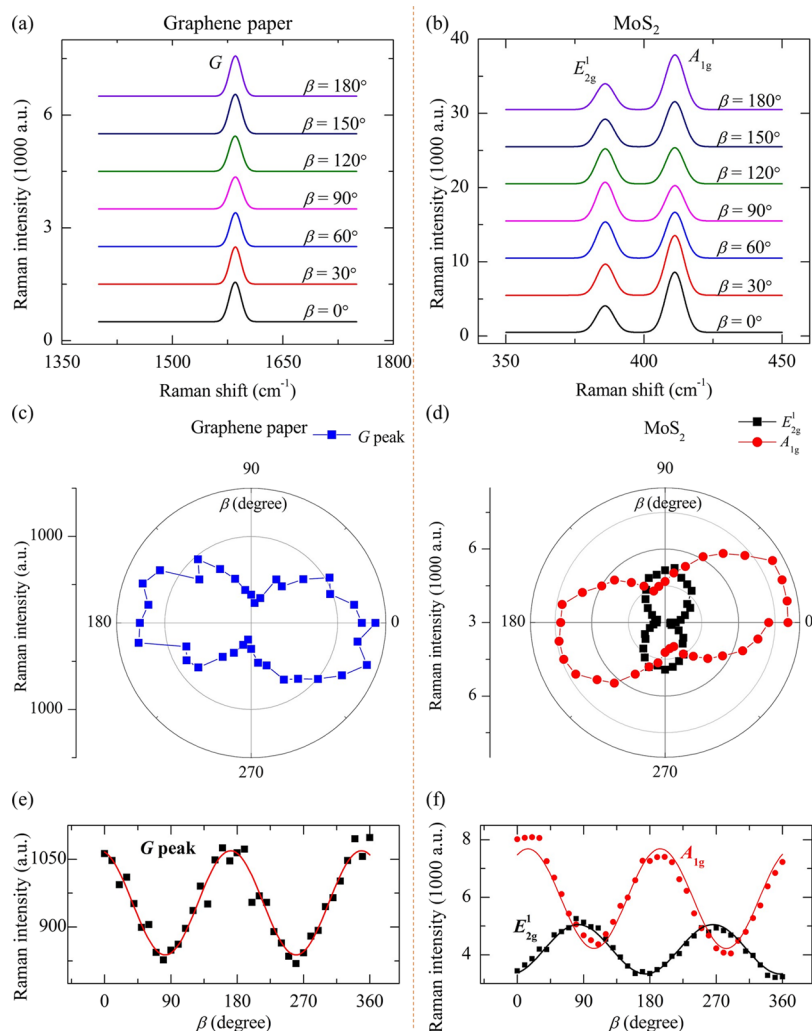
Results of the MoS<sub>2</sub> experiment are plotted in Figure 8a–c. Figure 8a shows the Raman spectrum of MoS<sub>2</sub> under different polarization angles. As  $\beta$  increases from 0 to 180°, the Raman intensity of the A<sub>1g</sub> mode first decreases until  $\beta = 90^\circ$ , and then it increases again. However, the Raman intensity of the E<sub>2g</sub><sup>1</sup> mode changes differently, and it reaches the maximum at  $\beta = 90^\circ$ . This behavior of two peaks is more obvious in the polar plot, as shown in Figure 8b. The polar plot of the Raman intensities of two peaks indicates the 90° phase difference between the E<sub>2g</sub><sup>1</sup> and A<sub>1g</sub> modes. Figure 8c shows the Raman intensity of each MoS<sub>2</sub> Raman peak against  $\beta$  as well as the fitting lines using the sine-squared function.  $\psi$ ,  $\phi$ , and  $\delta$  of the MoS<sub>2</sub> sample are measured and indicated in Table 1.

Figure 8d shows several representative Raman spectra of graphene paper at different  $\beta$  and room temperature. The polar plot of the Raman intensity of the G peak and fitted data using the sine-squared function are shown in Figure 8e,f, respectively. The result of this measurement is included in Table 1. Note that, by using this sample, it is only possible to measure  $\psi$  using the G peak.

As indicated by Table 1,  $\psi$  values of WS<sub>2</sub>, MoS<sub>2</sub>, and graphene paper are in very good agreement with each other and are around 0.85. Any discrepancy between the  $\psi$  measured using WS<sub>2</sub> sample and two other samples could be caused by



**Figure 7.** Measured  $\psi$  (left vertical axis),  $\phi$  (middle vertical axis), and  $\delta$  (right vertical axis) for (a) supported and (b) suspended WS<sub>2</sub> samples. The increasing (decreasing) trend in  $\psi$  ( $\delta$ ) by increased temperature is caused by the effects of the 2LA(M) mode Raman intensity change against sample temperature.



**Figure 8.** Room-temperature polarized Raman experiment using MoS<sub>2</sub> and graphene paper. Seven representative Raman spectra of (a) MoS<sub>2</sub> and (d) graphene paper at different polarization angles are presented. Polar plots of Raman intensities for (b) E<sub>2g</sub><sup>1</sup> and A<sub>1g</sub> peaks of MoS<sub>2</sub> and (e) G peak of graphene paper. There is an around 80° phase difference between the polar plots of the E<sub>2g</sub><sup>1</sup> peak and A<sub>1g</sub> or G mode. Fitting results of this experiment using (c) MoS<sub>2</sub> and (f) graphene paper. The fitting function is similar to the sine-squared function used to fit the WS<sub>2</sub> experiment results.

the quality of data fitting. As mentioned earlier, the 2LA(M) and E<sub>2g</sub><sup>1</sup> peaks of WS<sub>2</sub> overlap at our working temperature, and as a result, it causes some uncertainty in data analysis. In addition, transmission and reflection of a specific beam splitter vary with the light wavelength. In this work, since the wavelength of incident laser is always 532 nm, there will be no difference between the reflectivity of the beam splitter. Meanwhile, for the scattered light, which corresponds to  $\delta$ , transmission of the beam splitter could be different for different Raman modes of WS<sub>2</sub>, MoS<sub>2</sub>, and graphene. This is another reason for discrepancy between  $\delta$  values in Table 1. Additionally, there is an around 80° phase difference between the polar plot of the E<sub>2g</sub><sup>1</sup> mode of MoS<sub>2</sub> and polar plot of the G peak. This difference could be caused by the assumption that elements of Raman tensors of the E<sub>2g</sub><sup>1</sup> mode are equal (eq 3). Neglecting this assumption will result in a phase shift inside the sine-squared function. To evaluate this claim, the Raman intensity of the E<sub>2g</sub><sup>1</sup> mode is calculated by considering its Raman tensors with different elements as

$$I_{E_{2g}^1} \propto [(C \cos 2\alpha)(Ac + Bd) + (C \sin 2\alpha)(Ad - Bc)]^2 \cos^2 \beta + [(D \cos 2\alpha)(Ad - Bc) + (C \sin 2\alpha)(-Ac - Bd)]^2 \sin^2 \beta \quad (8)$$

As shown in eq 8, the Raman intensity of the E<sub>2g</sub><sup>1</sup> mode is not only a function of  $\beta$  but also  $\alpha$ . Regarding the E<sub>2g</sub><sup>1</sup> peak of the WS<sub>2</sub> sample, its phase shift is in between the G peak and E<sub>2g</sub><sup>1</sup> peak of MoS<sub>2</sub>, and as temperature goes higher, it becomes closer to MoS<sub>2</sub>. Theoretically, its phase shift should be similar to the MoS<sub>2</sub> sample. Again, this difference could be caused by the effect of the 2LA(M) mode on the data fitting. However, the Raman intensity of the 2LA(M) mode is weaker at higher temperatures,<sup>27</sup> and the polar plot of the E<sub>2g</sub><sup>1</sup> mode of WS<sub>2</sub> is expected to be similar to the MoS<sub>2</sub> polar plot at very high temperatures.

So far, we have discussed about the effects of sample preparation, working temperature, and beam splitter on polarized Raman spectroscopy. Note that aforementioned optical effects depend on the optical properties of the configuration and will affect the polarized Raman intensity regardless of the material. Therefore, these effects need to be considered for other materials, such as silicon, carbon

nanotubes, and black phosphorus. Especially in applications like identifying the crystalline orientation of black phosphorus, it is critical to consider these effects for more accurate analysis. For silicon, since it is not perfectly isotropic and could have different behaviors in both s- and p-polarized directions, these optical effects could affect the final polarized Raman intensity. Also, regarding carbon nanotubes, they have different polarization behaviors in the axial and radial directions, so the effects discussed in this paper should be considered in detail. Meanwhile, there is another point that needs to be taken into consideration, and that is the grating sensitivity for the two polarization directions. As shown in Figure 1a2, grating diffracts light into several beams in different directions. Raman intensities in both s- and p-polarized directions ideally should be the same for a specific grating configuration, but practically, they are not. However, grating reflectivity depends on polarization, detecting wavelength, groove density, and groove profile. In this work, the last three factors have a less effect on accuracy of this measurement, while the polarization effect is more important.

#### 4. CONCLUSIONS

In this work, few-layered WS<sub>2</sub> and MoS<sub>2</sub> as well as bulk graphene paper were used for studying their intensity responses to polarized Raman excitation laser. It was reported in previous works that Raman intensities of the E<sub>2g</sub><sup>1</sup> and G modes are independent of the polarization angle and do not change with  $\beta$ , while a strong dependency on  $\beta$  was discovered in this work for all three materials. The E<sub>2g</sub><sup>1</sup> and A<sub>1g</sub> Raman modes of nanometer-thick WS<sub>2</sub> and MoS<sub>2</sub> samples as well as the G Raman peak of bulk graphene were used to investigate the polarization dependency of the Raman intensity for each mode. The incident laser was polarized using a polarizer before irradiating the sample. Using the WS<sub>2</sub> sample, we investigated the effect of temperature and sample structure on the polarized Raman signal. The polarized Raman experiment was conducted on both supported and suspended areas of exfoliated WS<sub>2</sub>. These experimental data were verified and fitted by the classical theory of Raman scattering, which considers the polarization direction of the incident laser, different vibrational modes regarding each Raman mode, and rotation of the beam splitter about the z axis. It was conclusive that the Raman intensity variation with incident laser polarization is a function of the polarization angle ( $\beta$ ) and includes information about optical components of the Raman system, especially the beam splitter.

#### AUTHOR INFORMATION

##### Corresponding Authors

\*E-mail: zhangqianying526@163.com. Tel: 011-86-13647662074 (Q.Z.).

\*E-mail: xwang3@iastate.edu. Tel: 001-515-294-8023 (X.W.).

##### ORCID

Xinwei Wang: 0000-0002-9373-3750

##### Author Contributions

<sup>||</sup>H.Z. and R.W. contributed equally to this work.

##### Notes

The authors declare no competing financial interest.

#### ACKNOWLEDGMENTS

Financial support of this work by the College of Engineering of Iowa State University is gratefully acknowledged.

#### REFERENCES

- (1) Ferrari, A. C.; Meyer, J. C.; Scardaci, V.; Casiraghi, C.; Lazzeri, M.; Mauri, F.; Piscanec, S.; Jiang, D.; Novoselov, K. S.; Roth, S.; Geim, A. K. Raman Spectrum of Graphene and Graphene Layers. *Phys. Rev. Lett.* **2006**, *97*, 187401.
- (2) Malard, L. M.; Nilsson, J.; Elias, D. C.; Brant, J. C.; Plentz, F.; Alves, E. S.; Castro Neto, A. H.; Pimenta, M. A. Probing the Electronic Structure of Bilayer Graphene by Raman Scattering. *Phys. Rev. B* **2007**, *76*, 201401.
- (3) Wang, Y.; Cong, C.; Qiu, C.; Yu, T. Raman Spectroscopy Study of Lattice Vibration and Crystallographic Orientation of Monolayer MoS<sub>2</sub> under Uniaxial Strain. *Small* **2013**, *9*, 2857–2861.
- (4) Lu, X.; Luo, X.; Zhang, J.; Quek, S. Y.; Xiong, Q. Lattice Vibrations and Raman Scattering in Two-Dimensional Layered Materials Beyond Graphene. *Nano Res.* **2016**, *9*, 3559–3597.
- (5) Kim, Y.; Jhon, Y. I.; Park, J.; Kim, J. H.; Lee, S.; Jhon, Y. M. Anomalous Raman Scattering and Lattice Dynamics in Mono- and Few-Layer WTe<sub>2</sub>. *Nanoscale* **2016**, *8*, 2309–2316.
- (6) Wang, R.; Zobeiri, H.; Lin, H.; Qu, W.; Bai, X.; Deng, C.; Wang, X. Anisotropic Thermal Conductivities and Structure in Lignin-Based Microscale Carbon Fibers. *Carbon* **2019**, *147*, 58–69.
- (7) Xie, Y.; Han, M.; Wang, R.; Zobeiri, H.; Deng, X.; Zhang, P.; Wang, X. Graphene Aerogel Based Bolometer for Ultrasensitive Sensing from Ultraviolet to Far-Infrared. *ACS Nano* **2019**, *13*, 5385–5396.
- (8) Zobeiri, H.; Wang, R.; Wang, T.; Lin, H.; Deng, C.; Wang, X. Frequency-Domain Energy Transport State-Resolved Raman for Measuring the Thermal Conductivity of Suspended Nm-Thick MoSe<sub>2</sub>. *Int. J. Heat Mass Transfer* **2019**, *133*, 1074–1085.
- (9) Wang, R.; Wang, T.; Zobeiri, H.; Yuan, P.; Deng, C.; Yue, Y.; Xu, S.; Wang, X. Measurement of the Thermal Conductivities of Suspended MoS<sub>2</sub> and MoSe<sub>2</sub> by Nanosecond ET-Raman without Temperature Calibration and Laser Absorption Evaluation. *Nanoscale* **2018**, *10*, 23087–23102.
- (10) Zobeiri, H.; Wang, R.; Zhang, Q.; Zhu, G.; Wang, X. Hot Carrier Transfer and Phonon Transport in Suspended Nm WS<sub>2</sub> Films. *Acta Mater.* **2019**, *175*, 222–237.
- (11) Park, B.-w.; Jain, S. M.; Zhang, X.; Hagfeldt, A.; Boschloo, G.; Edvinsson, T. Resonance Raman and Excitation Energy Dependent Charge Transfer Mechanism in Halide-Substituted Hybrid Perovskite Solar Cells. *ACS Nano* **2015**, *9*, 2088–2101.
- (12) Leray, A.; Clément, J.-E.; Bouhélier, A.; Finot, E. Conformational Changes and Charge Transfer in Biomolecules Resolved Using Dynamic Enhanced Raman Correlation Spectroscopy. *J. Phys. Chem. B* **2019**, *123*, 1931–1938.
- (13) Zhao, Y.; Qiao, J.; Yu, P.; Hu, Z.; Lin, Z.; Lau, S. P.; Liu, Z.; Ji, W.; Chai, Y. Extraordinarily Strong Interlayer Interaction in 2D Layered PtS<sub>2</sub>. *Adv. Mater.* **2016**, *28*, 2399–2407.
- (14) Wang, T.; Liu, J.; Xu, B.; Wang, R.; Yuan, P.; Han, M.; Xu, S.; Xie, Y.; Wu, Y.; Wang, X. Identifying the Crystalline Orientation of Black Phosphorus by Using Optothermal Raman Spectroscopy. *ChemPhysChem* **2017**, *18*, 2828–2834.
- (15) Xia, J.; Li, X.-Z.; Huang, X.; Mao, N.; Zhu, D.-D.; Wang, L.; Xu, H.; Meng, X.-M. Physical Vapor Deposition Synthesis of Two-Dimensional Orthorhombic Sns Flakes with Strong Angle/Temperature-Dependent Raman Responses. *Nanoscale* **2016**, *8*, 2063–2070.
- (16) Congeduti, A.; Nardone, M.; Postorino, P. Polarized Raman Spectra of a Single Crystal of Iodine. *Chem. Phys.* **2000**, *256*, 117–123.
- (17) Kim, J.; Lee, J.-U.; Lee, J.; Park, H. J.; Lee, Z.; Lee, C.; Cheong, H. Anomalous Polarization Dependence of Raman Scattering and Crystallographic Orientation of Black Phosphorus. *Nanoscale* **2015**, *7*, 18708–18715.
- (18) Lee, J.-U.; Seck, N. M.; Yoon, D.; Choi, S.-M.; Son, Y.-W.; Cheong, H. Polarization Dependence of Double Resonant Raman Scattering Band in Bilayer Graphene. *Carbon* **2014**, *72*, 257–263.
- (19) Wu, J.; Mao, N.; Xie, L.; Xu, H.; Zhang, J. Identifying the Crystalline Orientation of Black Phosphorus Using Angle-Resolved

Polarized Raman Spectroscopy. *Angew. Chem., Int. Ed.* **2015**, *54*, 2366–2369.

(20) Lu, Z. Q.; Quinn, T.; Reehal, H. S. Polarization-Dependent Raman Spectra of Thin Crystalline Silicon Films. *J. Appl. Phys.* **2005**, *97*, No. 033512.

(21) Duesberg, G. S.; Loa, I.; Burghard, M.; Syassen, K.; Roth, S. Polarized Raman Spectroscopy on Isolated Single-Wall Carbon Nanotubes. *Phys. Rev. Lett.* **2000**, *85*, 5436.

(22) Zhang, S.; Yang, J.; Xu, R.; Wang, F.; Li, W.; Ghufuran, M.; Zhang, Y.-W.; Yu, Z.; Zhang, G.; Qin, Q.; Lu, Y. Extraordinary Photoluminescence and Strong Temperature/Angle-Dependent Raman Responses in Few-Layer Phosphorene. *ACS Nano* **2014**, *8*, 9590–9596.

(23) Ribeiro, H. B.; Pimenta, M. A.; De Matos, C. J. S.; Moreira, R. L.; Rodin, A. S.; Zapata, J. D.; De Souza, E. A. T.; Castro Neto, A. H. Unusual Angular Dependence of the Raman Response in Black Phosphorus. *ACS Nano* **2015**, *9*, 4270–4276.

(24) Wang, T.; Wang, R.; Yuan, P.; Xu, S.; Liu, J.; Wang, X. Interfacial Thermal Conductance between Mechanically Exfoliated Black Phosphorus and SiO<sub>x</sub>: Effect of Thickness and Temperature. *Adv. Mater. Interfaces* **2017**, *4*, 1700233.

(25) Yuan, P.; Wang, R.; Tan, H.; Wang, T.; Wang, X. Energy Transport State Resolved Raman for Probing Interface Energy Transport and Hot Carrier Diffusion in Few-Layered MoS<sub>2</sub>. *ACS Photonics* **2017**, *4*, 3115–3129.

(26) Fan, J.-H.; Gao, P.; Zhang, A.-M.; Zhu, B.-R.; Zeng, H.-L.; Cui, X.-D.; He, R.; Zhang, Q.-M. Resonance Raman Scattering in Bulk 2H-MS<sub>2</sub> (M= Mo, W; X= S, Se) and Monolayer MoS<sub>2</sub>. *J. Appl. Phys.* **2014**, *115*, No. 053527.

(27) Huang, X.; Gao, Y.; Yang, T.; Ren, W.; Cheng, H.-M.; Lai, T. Quantitative Analysis of Temperature Dependence of Raman Shift of Monolayer WS<sub>2</sub>. *Sci. Rep.* **2016**, *6*, 32236.

(28) Saito, R.; Tatsumi, Y.; Huang, S.; Ling, X.; Dresselhaus, M. S. Raman Spectroscopy of Transition Metal Dichalcogenides. *J. Phys.: Condens. Matter* **2016**, *28*, 353002.

(29) Mitioglu, A. Probing the Electronic Properties of Bulk and Monolayer Crystals of Tungsten Dichalcogenides Using Magneto-Spectroscopy. Ph.D. Thesis, Université Toulouse 3 Paul Sabatier (UT3 Paul Sabatier), 2015.